



Contents lists available at ScienceDirect

International Journal of Heat and Mass Transfer

journal homepage: www.elsevier.com/locate/ijhmt

Multi-artery heat-pipe spreader: Lateral liquid supply

G.S. Hwang^a, E. Fleming^b, B. Carne^c, S. Sharratt^d, Y. Nam^d, P. Dussinger^b, Y.S. Ju^d, M. Kaviany^{a,*}^a Department of Mechanical Engineering, University of Michigan, Ann Arbor, MI 48109, USA^b Advanced Cooling Technologies, Inc., Lancaster, PA 17601, USA^c Département Hydraulique et Mécanique des Fluides, ENSEEIHT, Toulouse, France^d Mechanical and Aerospace Engineering Department, University of California, Los Angeles, CA 90095, USA

ARTICLE INFO

Article history:

Received 15 September 2010

Received in revised form 7 January 2011

Accepted 7 January 2011

Available online 25 February 2011

Keywords:

Multi-artery

Evaporator

Heat pipe

Heat spreader

Meniscus recess

Capillary

Wick

Vapor chamber

Converging wick

ABSTRACT

We design and test a low thermal/hydraulic resistance, multi-artery heat-pipe spreader vapor chamber. Liquid (water) is supplied to a highly concentrated heat-source region through a monolayer evaporator wick and a set of lateral converging arteries, fabricated from sintered, spherical copper particles. The monolayer wick allows for a minimum evaporator resistance of $0.055 \text{ K}/(\text{W}/\text{cm}^2)$, which is related to a critical transition where the receding meniscus approaches the particle neck. Similar behavior is also observed in a monolayer-wick evaporator, partially submerged in liquid bath. After this minimum, local dryout occurs and increases the resistance. However, a continuous liquid supply through the lateral arteries does not allow for total dryout in the test limit of $580 \text{ W}/\text{cm}^2$. These thermal/hydraulic behaviors are predicted using the local thermal equilibrium and nonequilibrium models.

© 2011 Elsevier Ltd. All rights reserved.

1. Introduction

Limiting temperature of highly concentrated Joule-heating devices requires enhanced thermal management solutions. A common approach is to spread heat over a large area towards a sequential heat sink [1,2]. A vapor chamber acts as an idealized heat spreader with nearly isothermal and uniform heat spreading on evaporator wicks using liquid–vapor phase change. The dominant sources of its thermal resistance and heat removal limit are low thermal conductivity and large hydraulic resistance of the evaporator wick. Therefore, an optimal design of the evaporator wick is critical to the desired performance, e.g., evaporator resistance below $0.1 \text{ K}/(\text{W}/\text{cm}^2)$ with critical heat flux (CHF) on the order of $100 \text{ W}/\text{cm}^2$.

A variety of approaches have been employed using uniform thickness wicks, e.g., screen [3], sintered metal powders [1,2], and microfabricated posts [4]. Since thin uniform wicks can only deliver a limited liquid supply due to large hydraulic resistance, their CHF is rather low. On the other hand, thick wicks create a rather large evaporator resistance because of a long conduction path. To reduce both resistances, nonuniform thickness wicks, i.e., a thin uniform wick incorporated with thick liquid arteries, have been designed.

This decreases a thermal resistance through the thin wick, while it enhances CHF through the thick wick. Columnar, multiple arteries (posts) design, providing well-distributed liquid supply to the thin monolayer, has enhanced the vapor chamber performance, e.g., $q_{\text{CHF}} = 380 \text{ W}/\text{cm}^2$ and $A_h R_{k,e} = 0.05 \text{ K}/(\text{W}/\text{cm}^2)$ [5]. However, due to the limited spread of the liquid around the posts, a sudden, total dryout occurs. To increase the dryout limit, new artery design is needed. Also, the thin evaporator wick controls the minimum thermal resistance assisted by the receding meniscus inside it [4–6]. However, the thermal/hydraulic features associated with the receding meniscus have not been carefully analyzed.

Here, to increase the dryout limit, a lateral converging multi-artery heat pipe spreader (LC-MAHPS) with a monolayer evaporator wick is designed, fabricated and tested. We also analyze its thermal/hydraulic behavior, explaining the observed minimum evaporator resistance with thermal equilibrium and nonequilibrium models which are applied to heat flow adjacent to the three-phase contact line.

2. Fabrications and experiments

2.1. LC-MAHPS

The lateral converging multi-artery wick is incorporated into a copper/water vapor chamber for experimental characterization.

* Corresponding author. Tel.: +1 734 936 0402; fax: +1 734 647 3170.

E-mail address: kaviany@umich.edu (M. Kaviany).

Nomenclature

A	area (m^2)
d	diameter (m)
K	permeability (m^2)
Δh_{lg}	enthalpy of vaporization (J/kg)
k	thermal conductivity (W/m-K)
L	length (m)
q	heat flux (W/m^2)
r	radius (m)
T	temperature (K)
$\langle \rangle$	volume average

Greek symbols

ε	porosity
δ	thickness (m)
ρ	density (kg/m^3)
σ	surface tension (N/m)

Subscript

a	artery
CHF	critical heat flux
c	capillary
e	evaporator
f	fluid
h	heater
k	conduction
l	liquid
LD	local dryout
lg	liquid–gas phase change
m	monolayer
p	post or particle
s	solid
w <td>wick</td>	wick

The vapor chamber had the following dimensions: 4.8 mm × 7.6 cm × 12.7 cm with a 1 cm² heat input region as shown in Figs. 1(a) and (b). A sintered monolayer of spherical copper powder particles, approximately 60 μm in diameter, is used to feed liquid to release highly concentrated heat in the evaporator, while providing low thermal resistance. Since its liquid permeation is low due to the low permeability, a secondary feed structure, i.e., liquid artery, is required to prevent local dryout. These converging arteries extend over the top of the monolayer to minimize hydraulic pressure drop, while maximizing the available evaporation area

near the side surface of the arteries. The liquid arteries are sintered in-situ from spherical copper powders, approximately 100 μm in diameter. A thick, uniform wick is used outside (laterally) the evaporation region to deliver liquid to the arteries. Vapor space ensures that the vapor pressure drop is negligible.

This liquid-artery pitch design has been successful in enhancing critical heat flux by controlling the hydrodynamics stability of the liquid–vapor interface in pool boiling (liquid submerged wick) [7–9], and by creating distinct liquid supply (artery) and evaporator (monolayer) wicks [5,10,11]. Here we propose lateral liquid wick arteries to increase a dryout limit, while maintaining low thermal resistance through the monolayer wick.

The thermal/hydraulic characteristics of the vapor chamber are tested in a gravity neutral orientation as shown in Fig. 2. Condensers are placed on both edges of the top surface without wick. No condenser wick is needed as condensate pools at the bottom of the vapor chamber and then returns to the evaporator via the LC feed structure (thick uniform wick). For a general description of the test apparatus and testing methods are given in our previous work [5]. New to this test apparatus is the use of two separate liquid cooled heat sinks placed on the edges of the vapor chamber instead of one single heat sink spanning the whole surface opposite the evaporator. This approach was chosen to represent cold rail applications but the impact on the evaporator resistance has been shown insignificant. The vapor temperature is set to $T = 90$ to 95 °C during the test at the atmospheric pressure, while controlling the input heat flux by $q = \pm 25$ to 50 W/cm². The thermal/hydraulic characteristics of the vapor chamber are also sensitive to the liquid charge. Decreasing the charge reduces the thermal resistance, due to the smaller, effective liquid-filled wick thickness. However, it also results in a lower critical heat flux. Here, we use a 3 g liquid fill for a fully-flooded evaporator and artery wicks.

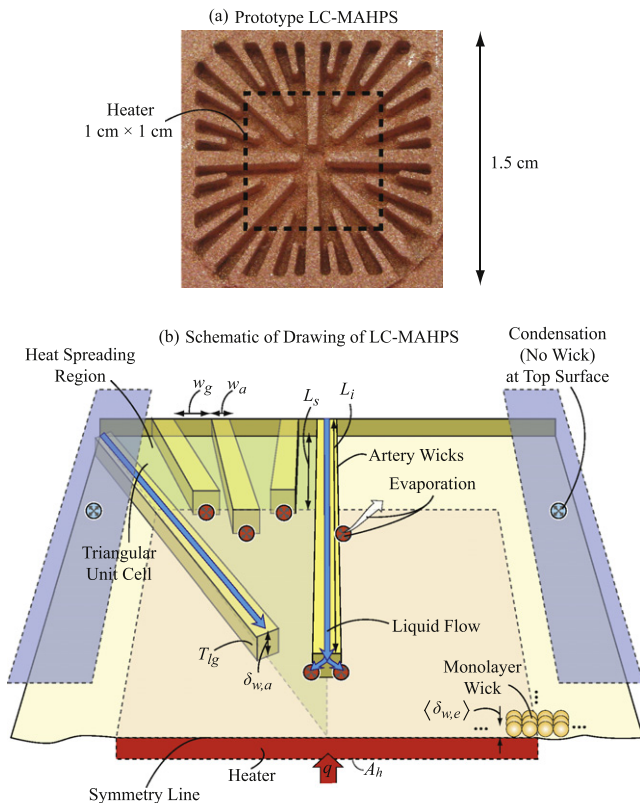


Fig. 1. (a) An image of a prototype LC-MAHPS. (b) A schematic of LC-MAHPS showing the thin evaporator monolayer wick and a set of lateral-converging liquid arteries. Phase change, heat, liquid and vapor flow paths, and key dimensions are illustrated. Condensation (no wick) at the side edges of top surface is also shown.

2.2. Monolayer evaporator wick: Meniscus recess

The thermal/hydraulic characteristics of the monolayer wick are also tested partially submerged in a liquid bath. The wick is comprised of Cu spheres, having a nominal diameter of approximately 60 μm with a standard deviation of ±4.5 μm, and average distance among the particles is 63 μm, as measured by an SEM image analysis as shown in Fig. 3(a). The spheres are sintered onto a 3 cm × 3 cm × 500 μm Cu substrate for 1 h at 960 °C. A 5 mm × 5 mm Au thin-film heater on a 100 μm Si wafer is soldered onto the back of the sample using a 100 μm layer of solder (thermal conductivity $k_s \sim 64$ W/m-K). To measure the heater tempera-

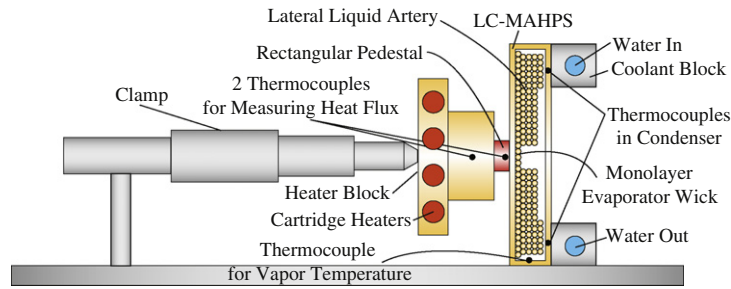


Fig. 2. A schematic drawing of the test section. The heater block, rectangular pedestal, CPMHPS, condenser water cooler, and thermocouple placements are also shown.

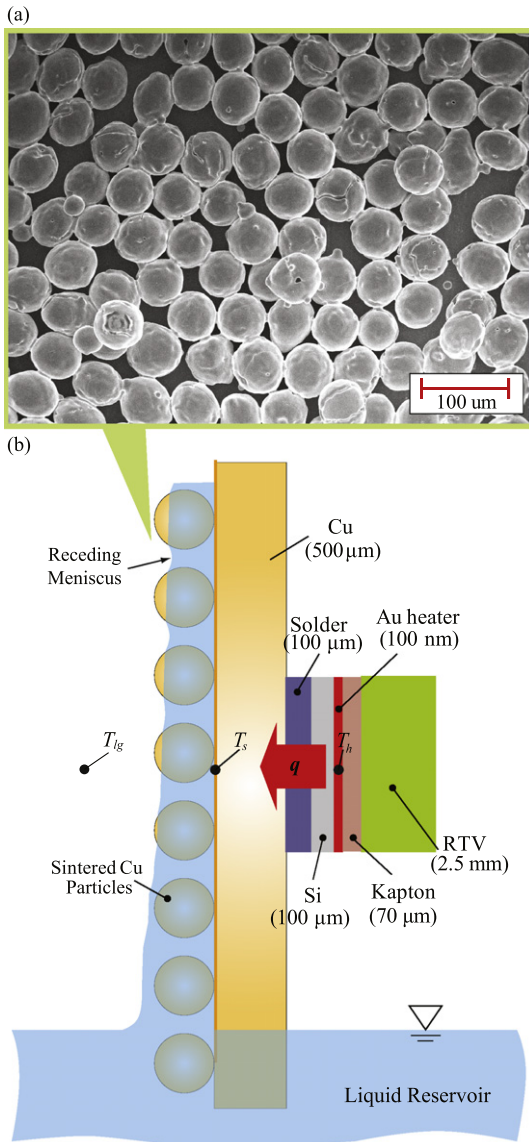


Fig. 3. (a) SEM image of the monolayer wick, average particle diameter of 58.5 μm with a standard deviation of ±4.5 μm, and solid fraction of 0.63. (b) A schematic of a vertically aligned, wet monolayer wick on Si substrate. A heater installed with a solder, Kapton, and RTV, and the placements of the thermocouples.

ture, a K-type thermocouple is bonded to the heater surface with a bead of OmegaBond 101, and it is electrically insulated from the heater using a 70 μm-thick Kapton tape. To thermally isolate the heater from the ambient, a 2.5 mm-thick silicone rubber (RTV 106) layer covers the entire back side of the heater surface.

The monolayer wick is tested in a vertical orientation (perpendicular to the liquid reservoir) as shown in Fig. 3(b), and the wick is

spontaneously wet by capillary suction before the heater power is turned on. Note that the effective wick (liquid) thickness is smaller at the top (smaller meniscus radius of curvature) compare to the bottom where meniscus extends into the liquid bath. The center of the heater is located 1 cm above the liquid reservoir. Filtered de-ionized water is degassed by boiling in the ambient air for approximately 4 h prior to the experiment. The Cu vacuum chamber is temperature/pressure controlled by flowing cooling water from a thermal bath (Thermoscientific, RTE 7) through copper condenser coils attached to the chamber. The target saturation temperature was ~43 °C. Detailed descriptions on the experimental setup/protocol are found in our previous work [4]. Heat flux applied to the wick is gradually increased by raising the DC voltage using a computer control system. Each voltage step is maintained for approximately 10 min to ensure steady states have been reached. The average (over the last 1 min of each step) temperature and heat flux are used for the data analysis. The dominant measurement uncertainties are from the thermocouples (±0.3 K). Note that the input power is measured using precision multi-meters (Keithly 2000 and 2400) for electric potential and current, respectively [0.0045% × (V) + 0.0006% × (100 V), and 0.0005%(A) ± 6.0 μA], and the measurement uncertainty of the heater power is negligibly small.

3. Meniscus recess and evaporation resistance models

Performance of the wet monolayer wick, thermal resistance and local dryout, is controlled by its receding meniscus as the capillary pressure increases, i.e., the heat flux increases. Here, we use local thermal equilibrium and nonequilibrium thermal/hydraulic models to explore and predict this performance.

3.1. Local thermal equilibrium model

In this model, the wet monolayer wick is treated as a homogeneous porous medium with local thermal equilibrium between the solid (copper particles) and liquid (water) phases. This allows using an effective wick thermal conductivity. Then, as the capillary pressure increases and liquid meniscus moves toward the heated surface, the effective wick thickness reduces. This in turn decreases the wick thermal resistance. Fig. 4(a) shows the schematic of wet monolayer wick with a uniform particle distribution. The meniscus is idealized with spherical curvature (two equal principal radii) joining three adjacent particles, with a contact angle. The radius of curvature is related to the spacing between the particles L_p , particle diameter d_p , and contact angle θ_c as

$$r_c = \frac{\frac{2}{3^{1/2}} L_p - d_p \sin \theta}{2 \sin(\theta - \theta_c)}, \quad (1)$$

$$\langle \delta_{w,e} \rangle = \frac{1}{2} \{ d_p (1 + \cos \theta) - r_c [1 - \cos(\theta - \theta_c)] \}, \quad (2)$$

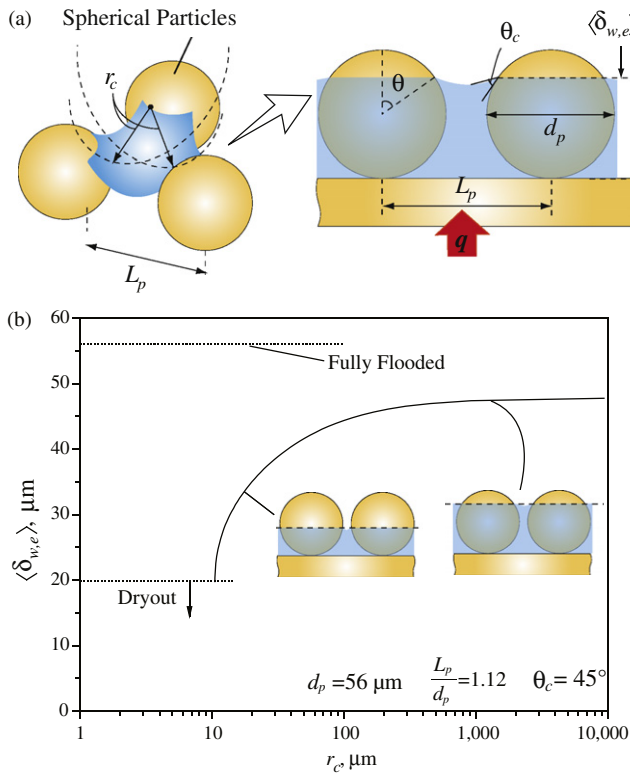


Fig. 4. (a) A schematic of the wet monolayer wick. The spherical particle diameter, spacing between particles, contact angle, effective wick thickness, and capillary meniscus radius are also shown. (b) Variations of the predicted effective thickness of the wet monolayer as a function of capillary meniscus radius, r_c . The effective thicknesses at the flooded and near dryout wick are also shown.

where $\theta_c < \theta < \theta_{max}$, and θ_{max} corresponds to $r_{c,min}$. The parameters from SEM image [Fig. 3(a)], are $\langle d_p \rangle = 56 \mu\text{m}$ and $L_p/d_p = 1.12$, and we use previously measured value of $\theta_c = 45^\circ$ [5]. These are summarized in Table 1. L_p is related to a porosity ε (which is critical to the effective thermal conductivity and permeability), through

$$\varepsilon = 1 - \frac{2\pi}{3^{1/2} L_p^2 \langle \delta_{w,e} \rangle} \left[\frac{2}{3} \left(\frac{d_p}{2} \right)^3 + \left(\frac{d_p}{2} \right)^2 \left(\langle \delta_{w,e} \rangle - \frac{d_p}{2} \right) - \frac{1}{3} \left(\langle \delta_{w,e} \rangle - \frac{d_p}{2} \right)^3 \right]. \quad (3)$$

Then $L_p/d_p = 1.12$ corresponds to $\varepsilon = 0.52$. We use a constant effective thermal conductivity by the available correlation for the half-diameter region adjacent to planar surface, i.e., $\langle k_{w,m} \rangle = 3.94 \text{ W/m-K}$ [12].

Using Eqs. (1) and (2), the variations of the average liquid-layer thickness $\langle \delta_{w,e} \rangle$ as a function of meniscus curvature r_c , are shown in Fig. 4(b). The thickness decreases with an increase in the capillary pressure (or decrease in r_c). This proceeds until the meniscus contact line approaches the particles neck region, and a sudden transition occurs (infinite slope or dryout, where $d \langle \delta_{w,e} \rangle / d r_c = 0$). Here, we set this to be an onset of the local dryout.

Table 1
Summary of the parameters used in the local thermal equilibrium model.

Parameters	Magnitude
$\langle k_{w,m} \rangle$	3.94 W/m-K
d_p	56 μm
L_p/d_p (ε)	1.12 (0.52)

For CHF, the available viscous-capillary liquid limit model [10,13] is used to predict the lateral local dryout. The dryout occurs where the viscous liquid pressure drop exceeds a given capillary pumping capability, given as

$$q_{CHF} = \frac{2\sigma \cos \theta_c \rho_l}{r_c \mu_l} \left(\frac{L_{e,a}}{K_a A_a} + \frac{L_{e,m}}{K_m A_m} \right)^{-1} \frac{\Delta h_{lg}}{A_h}, \quad (4)$$

where σ is the surface tension, ρ_l is the liquid density, μ_l is the liquid viscosity, $L_{e,a}$ and $L_{e,m}$ are the effective liquid traveling length both in the liquid arteries and the monolayer wicks, K_a and K_m are the permeability of the liquid artery and monolayer wicks, and A_a and A_m are the cross section area of the liquid artery and the monolayer wicks, and A_h is the heated area, and Δh_{lg} is the heat of evaporation. $L_{e,m} = 1 \text{ mm}$ is used (the spacing between the arteries, Fig. 1). Gravity is ignored due to a negligibly small bond number.

The liquid pressure drop in the monolayer wick is dominant over that in the liquid artery wicks, due to low permeability (its small particle size) and small cross section area. Note that q_{CHF} is calculated using the liquid pressure drop only through the four longest liquid arteries ($L_{e,a} = 8.4 \text{ mm}$), where are critical to liquid supply to the onset of the lateral local dryout. The meniscus recess is beneficial to the capillary pumping capability due to the small meniscus radius near the bottle neck, while it is unfavorable to the effective liquid permeation through the monolayer wick due to the reduced cross section area.

The thermal resistance is defined as the total heat flux divided by the wick superheat, and is proportional to the effective wick thickness (Fourier law) given as,

$$A_h R_k = \frac{\Delta T}{q} = A_h \left(\frac{\langle k_{w,m} \rangle A_{m,e}}{\langle \delta_{w,m} \rangle} + \frac{\langle k_{w,a} \rangle A_{a,e}}{\langle \delta_{w,a} \rangle} \right)^{-1}, \quad (5)$$

where $\Delta T = T_s - T_{lg}$ and $A_{m,e}$, $A_{a,e}$ are the evaporation surface areas in the monolayer and liquid arteries, $\langle \delta_{w,a} \rangle$ is the average heat flow path through the liquid arteries, i.e., $0.5 (\delta_{w,a} + w_a)^{1/2}$. Although the effective surface area is related to a combined area of the lateral heat spreading beyond the heated area and the extended surface area of the liquid arteries, here we used a fitted value using the resistance at low q and find $A_{m,e} = 0.812 A_h$ and $A_{a,e} = 0.588 A_h \text{ cm}^2$. After the local dryout (LD), a lateral local dryout occurs. This reduces effective evaporation area, which in turn increases the thermal resistance.

Further analyses of the liquid film morphology have been made using the surface energy minimization [14]. Our model elucidates the capillary meniscus recess and its relation to the observed decreasing thermal resistance and enhanced hydrodynamic limit.

3.2. Local thermal nonequilibrium model

In this model, the wet monolayer wick is treated as two highly-contrasting, thermal-conducting phases in local thermal nonequilibrium, i.e., solid-copper and liquid. The high thermal conductivity copper particles are the primary heat flow path, and this heat passes through the thin liquid film as shown in Figs. 5(a) and (b). The liquid has nearly two orders of magnitude lower thermal conductivity, so the liquid filling the pores is not the preferred heat flow path. Then, the dominant resistance is in the liquid body with surface evaporation, and this in turn is related to the capillary meniscus recess. Due to the high thermal conductivity, isothermal particles are assumed. The predictions confirm the decreasing thermal resistance prior to the local dryout in the experiment (as discussed later). These thin liquid film geometries are constructed using Eqs. (1), (2), and (4). Since the evaporation occurs at the liquid-vapor interface, we use the saturation temperature (function of vapor pressure). The heat flow rate between the substrate surface and the liquid-vapor interface saturation temperature is cal-

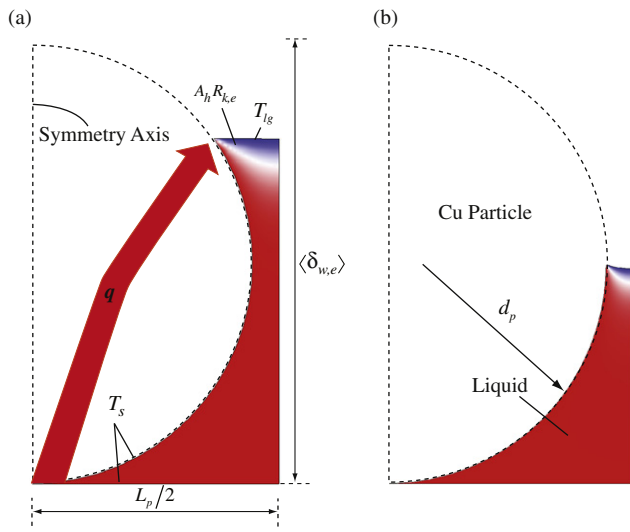


Fig. 5. Predicted temperature distribution in the liquid (cross section view of spherical particle, axisymmetric). The red color represents high temperature, whereas the blue color corresponds to low temperature. The heat flow path and the resistance through liquid $A_h R_{k,e}$, are also shown. (a) Fully-wet wick, and (b) half-filled wick.

culated using a commercial finite-element code and liquid film geometry (axisymmetry spherical particle-liquid shell), and then the local thermal resistance is predicted using the Fourier law. The used geometric parameters are listed in Table 1, and a constant liquid thermal conductivity $k_f = 0.7 \text{ W/m-K}$ (at $T = 95 \text{ }^\circ\text{C}$) is used. The total wick resistance is calculated using this local thermal resistance and $1.2A_h$, which allows for the heat spreading through the substrate (a 1 mm copper plate) [8].

The thermal oxidation creates a thin, oxide layer about $0.2 \text{ }\mu\text{m}$ on the wick surface, causing a thermal resistance. However, this resistance is small compared to that of the thicker liquid film.

4. Results and discussions

As discussed above, the monolayer evaporator wick design/performance is central to achieving a low thermal resistance. So, we discuss the monolayer evaporator wick experimental results, and then proceed with the multi-artery vapor chamber experimental results, and make a comparison with the model predictions.

4.1. Monolayer evaporator wick: Meniscus recess

Fig. 6(a) shows variations of the measured heat flux q with respect to the monolayer wick superheat $T_s - T_{lg}$ [Figs. 3(a) and (b)], and Fig. 6(b) shows that the corresponding wick thermal resistance as a function of q . At $q < 45 \text{ W/cm}^2$, the heat flux monotonically increases as the superheat increases, showing a decrease in the resistance monotonically from 0.24 to $0.10 \text{ K/(W/cm}^2\text{)}$. This is associated with the liquid level reduction by a receding meniscus until it reaches the minimum thickness of liquid, where the contact line is near a particle neck. At $q = 45 \text{ W/cm}^2$, a significant transition occurs as the minimum resistance is reached. It is caused by a sudden change in the receding liquid meniscus when the contact line approaches the particle neck. For $q > 45 \text{ W/cm}^2$, the receding meniscus hinders liquid flow and local dryout begins to occur. This in turn reduces the effective evaporation area, and increases the resistance, designated as a lateral local dryout. Note that the wick thermal resistance is defined as $A_h R_k = (T_s - T_{lg})/q$. The resistance is also used to calculate the effective monolayer wick thickness using a commercial finite element modeling tool, assuming a uniform

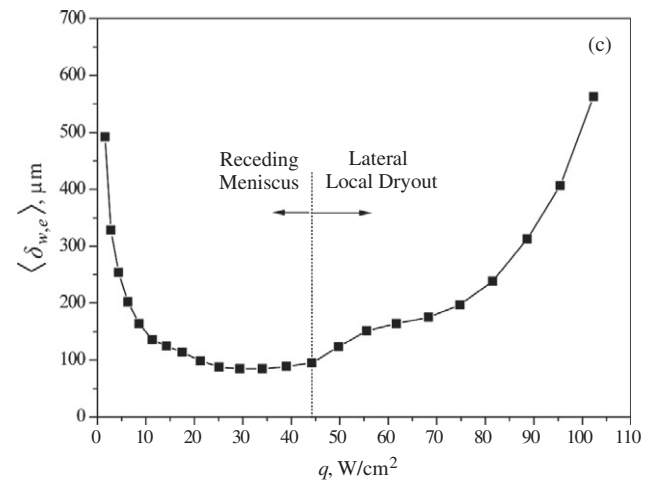
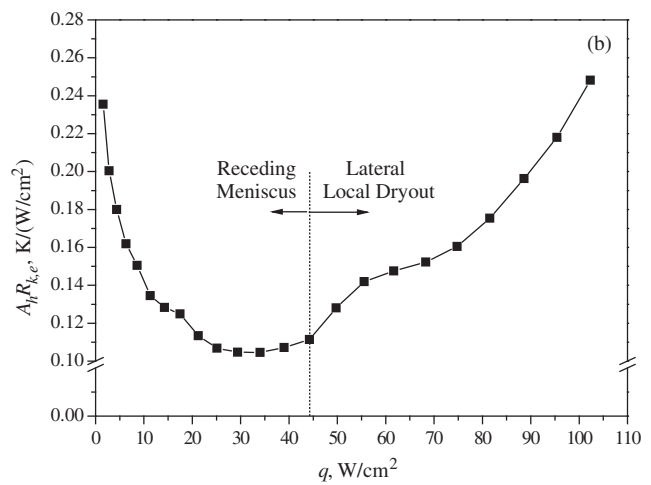
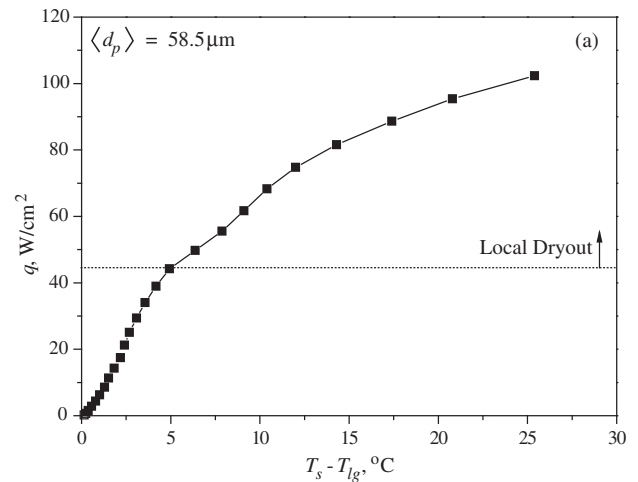


Fig. 6. (a) Variations of the heat flux as a function of the wick superheat, in the gravity monolayer wick. (b) Variations of the equivalent wick thermal resistance with respect to the wick superheat. (c) Variations of the effective monolayer thickness as a function of the heat flux. The receding meniscus and local dryout regimes are also shown.

effective monolayer thickness over a constant evaporation surface area and an effective wick thermal conductivity (Table 1), and the results are shown in Fig. 6(c) as a function of q . The predicted thickness is significantly greater than the particle diameter at $q > 45 \text{ W/cm}^2$, which is not physical. This large thickness corresponds to the reduced evaporation surface area by the lateral local dryout with-

out significant change of the thermal conductivity. Note that the minimum effective wick thickness is larger than that of the monolayer, and this is related to the large liquid film thickness at the bottom of the wick, due to liquid submersion [as shown in Fig. 3(b)].

4.2. LC-MAPHS

In the LC-MAHPS, the heat flux q is measured as a function of the wick superheat, as shown in Figs. 7(a) and (b). The experiments were repeated four times for reproducibility, and only one set of data is shown. At low $q < 350 \text{ W/cm}^2$, the wick superheat linearly increases with the heat flux, and then at $q > 350 \text{ W/cm}^2$ the wick superheat significantly increases. In Fig. 7(b), the decrease in the thermal resistance at $q < 350 \text{ W/cm}^2$ is caused by the thinning effective wick thickness, i.e., meniscus recess [Figs. 4(a) and (b)], and at near $q = 350 \text{ W/cm}^2$, the meniscus contact line is near a bottle neck of the wick. This constant thickness prevails over a range of heat flux, and in turn results in the minimum thermal resistance, $0.055 \text{ K/(W/cm}^2)$. At higher heat flux, a lateral local dryout occurs near the center of the heated region where the liquid supply is limited by the large hydraulic pressure drop, and the dryout laterally proceeds towards the edge of the heated region. Although this increases the thermal resistance, it leads to no complete dryout in

the test limit of $q = 580 \text{ W/cm}^2$, compared to the post artery design [5]. While maintaining minimal particle-size/pore-size distribution variations in the monolayer wick, the lateral design allows for a sustainable liquid supply at the high heat flux, whereas the post design results in a sudden, total dryout due to the limited spread of the liquid around the posts.

The prediction by the local thermal equilibrium model shows the thermal resistance decreases with the receding meniscus until the onset of the local dryout (LD) marked with $q_{LD} = 174 \text{ W/cm}^2$, and $T_s - T_{lg} = 12.8 \text{ K}$. After the onset of this local dryout, the resistance increases with the increase in the heat flux, and the predictions are in reasonable agreement with the experiment. Note that using the minimum wet wick thickness [at the minimum meniscus radius $r_{c,min}$ [Figs. 4(a) and (b)]], we find the low resistance limit. Note that the evaporator resistance in LC-MAHPS [Fig. 7(b)] is smaller than that in the submerged wick test [Fig. 6(b)], due to larger wet wick thickness close to the liquid bath. The local thermal nonequilibrium model predicts the thermal liquid resistance $A_h R_{k,e} = 0.072 \text{ K/(W/cm}^2)$ for $q \sim 0 \text{ W/cm}^2$, and $A_h R_{k,e} = 0.058 \text{ K/(W/cm}^2)$ for $q = 147.18 \text{ W/cm}^2$. Note that the particle-substrate contact and particle conduction resistances are neglected. Thus, this is the low limit, and in good agreement with the experiment.

4.3. Hysteresis

Hysteresis in the thermal resistance is observed as shown in Fig. 8. This is caused by liquid emptying (increasing q) and filling of the center of the pore throat, which in turn affect the effective wick thickness and the resulting resistance. In the increasing q branch, the contact line may anchor on top and not slip as meniscus recedes, while in the decreasing q branch the contact line moves up toward the pore throat as the pore is filled.

Although the exact capillary meniscus recess mechanisms including their relevance to the hysteresis are unknown, our non-equilibrium model predicts that the triple-phase contact at the center of the pore throat [Fig. 5(b)] allows for $q = 150 \text{ W/cm}^2$ [Fig. 7(a)]. This means that the local dryout begins where the contact line is below the center of the pore throat, and we postulate that the contact line passes through the pore throat prior to the onset of the local dryout (increasing q branch). The measured thermal resistances are higher than those in Fig. 7(b) at low heat flux, although the resistance decreases towards the minimum with increasing heat flux (onset of local dryout). At low heat flux, the liquid film is expected to be above the center of the pore throat, and

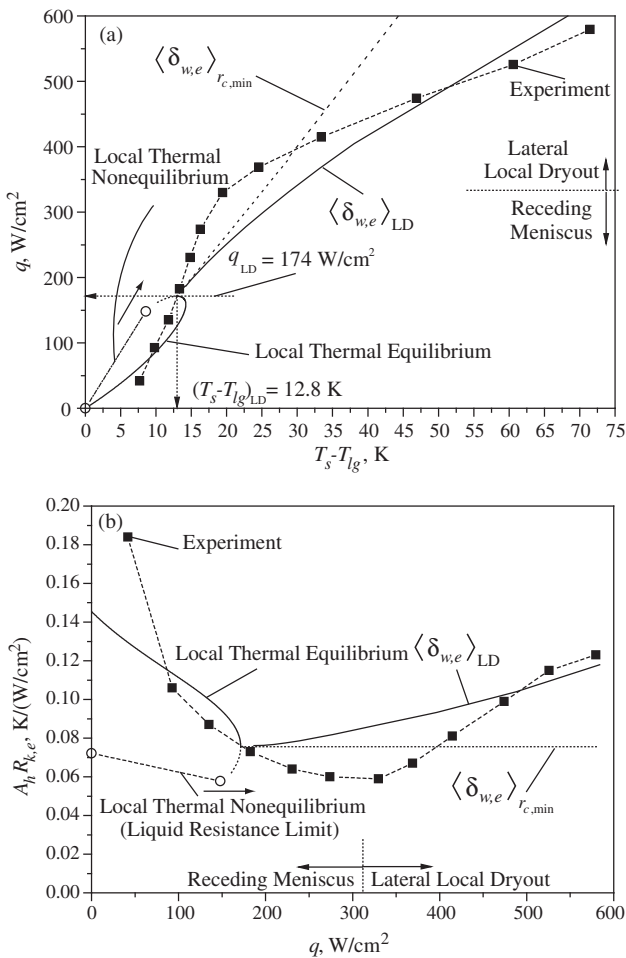


Fig. 7. (a) Variations of the measured and predicted heat flux q with respect to the wick superheat, $T_s - T_{lg}$ both in meniscus recess and lateral local dryout. The predictions are also shown for the constant effective wick thickness at the minimum, constant meniscus radius $r_{c,min}$, $\langle \delta_{w,e} \rangle$ at $r_{c,min}$, and lateral local dryout $\langle \delta_{w,e} \rangle_{LD}$. (b) Variations of the measured and predicted wick thermal resistances based on $\langle \delta_{w,e} \rangle$ at $r_{c,min}$ and $\langle \delta_{w,e} \rangle_{LD}$.

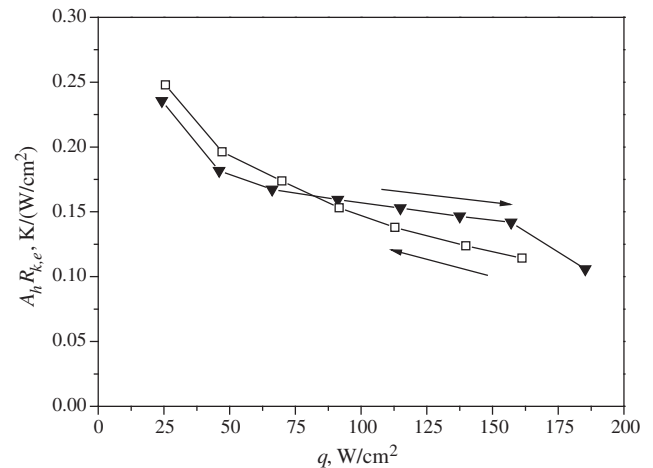


Fig. 8. Variations of the measured resistance $A_h R_{k,e}$ with respect to the heat flux q . Both increasing and decreasing the heat flux branches are shown.

the variation in the resistance is related to the capillary meniscus recess history, i.e., increase/decrease in heat flux and heterogeneous pore-throat structure.

5. Conclusion

A novel vapor chamber is designed for a low wick thermal resistance and high flux limit using a thin monolayer and lateral converging liquid artery wicks. The concentrated heat removal is achieved by enhanced liquid (water) supply through low hydraulic-resistance lateral arteries, and by a low thermal resistance through the receding meniscus, monolayer evaporator wick. Three major thermal/hydraulic characteristics are found and explained using the local equilibrium/non-equilibrium models. a) At low heat flux, the equilibrium receding meniscus model shows that the thermal resistance is related to the moving contact line of liquid within the wick, and the non-equilibrium model (liquid conduction only) reveals that the dominant heat flows through the very thin liquid layer at the triple phase contact line as the low resistance limit. These are in good agreement with the experimental results. b) After the local dryout, the resistance increases with the heat flux, due to the decreased evaporation surface area by a lateral recess of the wet monolayer (lateral local dryout). c) At high heat flux, the low hydraulic resistance through lateral liquid arteries increase very large global dryout limit, and it is not reached in the 580 W/cm² test limit.

Acknowledgement

This material is based upon work supported by the Defense Advanced Research Project Agency (DARPA) and Space and Naval Warfare Systems Center (SPAWARS-YSCEN), San Diego, CA under Contract No. N66001-08-C-2007. The views, opinions, and/or findings contained in this article/presentation are those of the author/

presenter and should not be interpreted as representing the official views or policies, either expressed or implied, of the DARPA or the Department of Defense.

References

- [1] D. Mehl, P. Dussinger, K. Grubb, Use of vapor chambers for thermal management, in: *National Electronic Packaging and Production Conference Proceedings of the Technical Program (East and West)* 3, (1999), 1358–1366.
- [2] S.-C. Wong, J.-H. Liou, C.-W. Chang, Evaporation resistance measurement with visualization for sintered copper-powder evaporator in operating flat-plate heat pipes, *Int. J. Heat Mass Transfer* 53 (2010) 3792–3798.
- [3] J.-H. Liou, C.-W. Chang, C. Chao, S.-C. Wong, Visualization and thermal resistance measurement for the sintered mesh-wick evaporator in operating flat-plate heat pipes, *Int. J. Heat Mass Transfer* 53 (2010) 1498–1506.
- [4] Y. Nam, S. Sharratt, G. Cha, Y.S. Ju, Characterization and modeling of the heat transfer performance of nanostructured Cu micropost wicks, submitted for publishing (2010).
- [5] G.S. Hwang, Y. Nam, E. Fleming, P. Dussinger, Y.S. Ju, M. Kaviany, Multi-artery heat pipe spreader: experiment, *Int. J. Heat Mass Transfer* 53 (2010) 2662–2669.
- [6] T. Semenic, I. Catton, Experimental study of biporous wicks for high heat flux applications, *Int. J. Heat Mass Transfer* 52 (2009) 5113–5121.
- [7] S.G. Lister, M. Kaviany, Pool-boiling CHF enhancement by modulated porous-layer coating: theory and experiment, *Int. J. Heat Mass Transfer* 44 (2001) 4287–4311.
- [8] D.H. Min, G.S. Hwang, Y. Usta, O.N. Cora, M. Koc, M. Kaviany, 2-D and 3-D modulated porous coatings for enhanced pool boiling, *Int. J. Heat Mass Transfer* 52 (2009) 2607–2613.
- [9] O.N. Cora, D.H. Min, M. Koc, M. Kaviany, Microscale-modulated porous coatings: fabrication and pool-boiling heat transfer performance, *J. Micromech. Microeng.* 20 (2010) 035020-1-9.
- [10] G.S. Hwang, M. Kaviany, W.G. Anderson, J. Zuo, Modulated wick heat pipe, *Int. J. Heat Mass Transfer* 50 (2007) 1420–1434.
- [11] D.H. Min, G.S. Hwang, M. Kaviany, Multi-artery, heat pipe spreader, *Int. J. Heat Mass Transfer* 52 (2009) 629–635.
- [12] K. Ofuchi, D. Kunii, Heat-transfer characteristics of packed beds with stagnant fluid, *Int. J. Heat Mass Transfer* 8 (1965) 749–757.
- [13] G. Peterson, *An Introduction to Heat Pipes: Modeling, Testing, and Applications*, Wiley, New York, 1994.
- [14] R. Ranjan, J.Y. Murthy, S.V. Garimella, Analysis of the wicking and thin-film evaporation characteristics of microstructures, *J. Heat Transfer* 131 (2009) 101001-1-11.